RSC Advances

PAPER

View Article Online
View Journal | View Issue

Cite this: *RSC Adv.*, 2017, **7**, 49309

One-pot synthesis of MoS_2/WS_2 ultrathin nanoflakes with vertically aligned structure on indium tin oxide as a photocathode for enhanced photo-assistant electrochemical hydrogen evolution reaction†

Xinxin Jiang, Baoliang Sun, Ye Song, Meiling Dou, Jing Ji* and Feng Wang *

Received 28th September 2017
Accepted 10th October 2017

DOI: 10.1039/c7ra10762e

rsc.li/rsc-advances

A hierarchical structure composed of vertically aligned ultrathin two dimensional (2D) MoS_2/WS_2 nanosheets is fabricated through a facile one-pot hydrothermal reaction. Scanning electron microscope (SEM), transmission electron microscope (TEM) and photoluminescence (PL) indicate that the MoS_2/WS_2 hybrid shows ultrathin nanoflakes with a thickness of 2–10 nm, and the as prepared heterostructure markedly enhances the separation of electro–hole pairs. Benefiting from the integrated W-doped MoS_2, the vertically aligned nanostructure exhibits a moderate degree of disorder and increased active surface area. Electrochemical measurements (cyclic voltammetry (CV), linear sweep voltammetry (LSC) and electrochemical impedance spectroscope (EIS) under light illumination or in dark) indicated that the MoS_2/WS_2 hybrid (especially the hybrid with Mo : W of 1/1) exhibits much better photo-and electrochemical performance than its counterpart of pure MoS_2 or WS_2, which made it a promising photocathode for electrocatalytic hydrogen evolution reaction (HER) by photo-assistance.

1. Introduction

Investigation of photoelectrocatalytic activities in transition metal dichalcogenides (TMDs) has revealed a new category of photonic nanomaterials with potential applications in hydrogen evolution reaction (HER).[1–16] These materials are characterized by a unique 2 dimensional (2D) structure of trigonal-prismatic metal centres with weak interlayer S–S bonding. Among the TMDs, WS_2 and MoS_2 have an analogous structure and share similar physical and chemical properties. Both are the most interesting layered materials for HER because their hydrogen binding energy is close to that of Pt-group metals,[17] and are considered as an alternative electrocatalyst to Pt-group metals towards the HER.[18–22] In addition, their graphene-like structure possesses direct band gaps corresponding well to visible-to-near-IR photon energies,[23] therefore, are much suitable in many optoelectronic applications.[24–26]

However, MoS_2 or WS_2 alone has negligible photocatalytic activity probably due to the fact that MoS_2 or WS_2 has a relative narrow band gap, and thus is liable to cause recombination of photoinduced electron–hole. Up to now, most of MoS_2 or WS_2 based photoelectrocatalyst reported for HER applications concerned with traditional photocatalytic materials (*e.g.*, MoS_2/CdS, WS_2/CdS,[27] MoS_2/Cu_2O,[28] MoS_2/graphene/CdS,[29] MoS_2/TiO_2 [30] *etc.*).

Theoretical calculations have shown that MoS_2/WS_2 heterostructures present an ideal energy band alignment of type-II semiconductors which is in favor of the separation of photoinduced electron–hole pairs.[31,32] And some investigations have quantitatively analysed and probed the model heterostructure MoS_2/WS_2 concerning with the 2D spatial distributions of the built in potential and the related electronic structure.[33,34] Therefore, the cocatalyst of coupling of MoS_2 with WS_2 has the potential in the applications of photocatalysis.

On the other hand, the photo-and electrocatalytic activities can be improved by ways of tuning the morphologies of TMDs. Since previous experiments[35–37] and density function theory studies[38] have shown that the edges of MoS_2 were identified as active sites for the HER, and both WS_2 and MoS_2 show morphology-dependent photo- and electrocatalytic activities,[39–43] a large body of work has been directed at design and control of the morphologies and microstructures. Specifically, the investigations focused on controllable growth of MoS_2 or WS_2 nanostructures, especially as nanoparticles and mono-or-fewer layers that maximally expose active edge sites to the reactants, and optimization of the number of active sites by elemental doping TMDs.[44–47]

State Key Laboratory of Chemical Resource Engineering, Beijing Key Laboratory of Electrochemical Process and Technology for Materials, Beijing University of Chemical Technology, Beijing 100029, China. E-mail: jijing@mail.buct.edu.cn; wangf@mail.buct.edu.cn

† Electronic supplementary information (ESI) available. See DOI: 10.1039/c7ra10762e

From the view point of electrocatalytic kinetics, vertically aligned 2D nanostructures on the conductive substrate is an ideal morphology for enhancing the photoelectrocatalytic activity due to their abundant active sites,[48] large specific surface and easy electron transportation. Many different synthesis methods for the preparation of vertically aligned TMD-based 2D structured materials have been explored. However, the preparation of vertically aligned 2D nanosheets usually grows on the carbon based[49,50] or porous substrate[51] through multi-step synthetic processes, which find an application only in electrocatalysis for HER. In addition, most photo or electrocatalysts are prepared in form of powder assemblies, and require binder to prepare the electrodes. The related photo- or eletrocatalytic reaction is conducted either under open-circuit conditions (the electron and hole transport at the same electrode) using power suspensions or catalyst fixed on a support (especially for the electrocatalyst for HER, which is generally used as the cathode), or alternatively in a photo-electrochemical setting in which bias potential is applied to enhance the photocurrent.

To make use of the integration of electro- and photocatalytic activities as a superior photoelectrocatalyst for PEC cells, vertically aligned nanostructure of ultrathin 2D MoS_2/WS_2 nanosheets which is directly grown on transparent indium tin oxide (ITO) substrates is very critical, since they are compatible with the direct photocatalytic applications. This hybrid structure not only favors light harvesting and adsorption, but also is beneficial to fast electron transportation, ion diffusion and sufficient electrochemical reaction of individual nanostructures due to enriched active sites and binder free combination.

In this work, hierarchical structures composed of vertically aligned ultrathin 2D MoS_2/WS_2 nanosheets were fabricated through a facile one-pot hydrothermal reaction. By this approach, the whole scale of vertically grown ultrathin MoS_2/WS_2 sheets was fabricated directly on ITO substrate. Herein, the hybrid nanosheets of MoS_2/WS_2 supplied numbers of active sites with proper defects since the elements of Mo and W doped with each other. More meaningful, favorable band alignment, as well as intimate p–n heterojunction between MoS_2 and WS_2, provides an effective carrier separation in this composite based photoelectric device. Consequently, the as-synthesized composites of MoS_2/WS_2 nanosheets shows better visible light activities than that of either pure WS_2 or MoS_2 nanostructures and shows great potential for integration of electro- and photocatalysis as a superior photoelectrocatalyst for PEC cells.

Up to now, the investigations on MoS_2/WS_2 composites mainly focused on the electronic structure of the model heterostructure, and little attention has been given to the influence of the as prepared nanostructures on their photo-and electrocatalytic activities. Among the few literatures related to the photoelectrocatalysis of RHE for MoS_2/WS_2 composites (Table 1), the photoelectrocatalytic activity is far from satisfactory, and still needs to be improved. The rational use of the MoS_2/WS_2 cathode provided a new avenue toward achieving an enhanced electrocatalytic activity by photo-assistance.

2. Experimental section

2.1. Materials

Sulfuric acid was purchased from Sinopharm Chemical Reagent Co., Ltd. Sodium molybdate dehydrate, sodium tungstate dehydrate and thioacetamide was obtained from J&K. Indium tin oxide (ITO) coated glass was purchased from China South Glass. Deionized water (resistivity > 18.4 MΩ cm^{-1}) was prepared using a pure water system (TTL-6B). All chemical reagents were used without further purification.

2.2. Preparation of MoS_2/WS_2 vertical mesh-shaped structure

A simple hydrothermal method was preferred to prepare the vertical aligned MoS_2/WS_2 ultrathin sheets on the ITO substrate. The ITO substrate was ultrasonically cleaned in acetone, ethanol and deionized (DI) water for 15 min each, respectively, prior to use. In a typical reaction, a 2 × 4 cm^2 area of the ITO substrate was placed vertically at the bottom of the Teflon-lined stainless-autoclave (25 ml) and immersed in a solution composing of 0.0086 mmol of $(NH_4)_6Mo_7O_{24}\cdot 4H_2O$, 0.06 mmol of $Na_2WO_4\cdot 2H_2O$ and 0.4 mmol of L-cystine. And then, the autoclave was sealed and thermally treated at 220 °C for 20 hours. The as-prepared sample of vertically aligned MoS_2/WS_2 hybrid nanosheets (labelled MoS_2/WS_2) was then removed from the solution, washed thoroughly with ethanol and distilled water, and dried naturally. In control experiments, the vertically aligned pristine MoS_2 and WS_2 structures on the ITO substrate were prepared by the similar hydrothermal method, respectively, with that of MoS_2/WS_2 nanosheets, except that the ITO is immersed in a solution composing of 0.0172 mmol $(NH_4)_6Mo_7O_{24}\cdot 4H_2O$, or 0.12 mmol $Na_2WO_4\cdot 2H_2O$ and 0.4 mmol L-cystine. In control experiments, the precursors of MoS_2 and WS_2 are stoichiometrically fed into the reaction system in mole ratio of 2 : 1, 1 : 1, and 1 : 2 for Mo/W, which is designated as the mole ratio of Mo and W (2 : 1), (1/1) and (1/2), respectively. It is notably that the concentration of $(NH_4)_6Mo_7O_{24}\cdot 4H_2O$ remains constant regardless of the mole ratio of Mo/W.

2.3. Characterization

Scanning electron microscopy (SEM) investigation was conducted by a JEOL-6701F field emission scanning electron microscope which is operated at a scanning current of 10 μA and an accelerating voltage of 5 kV. High resolution transmission electron microscopy (HRTEM) is performed by a JEOL JSM-3010 instrument operated at 200 kV. High-angle annular dark-field scanning transmission electron microscopy (HAADF-STEM) and corresponding energy dispersive spectroscopy (EDS) mapping analysis were carried out on a JEOL JEM-2010F STEM. The crystal phases of the samples were collected on an X-ray diffractometer with Cu–K radiation at a scan rate of 5° min^{-1} (Rigaku D/max-2500B2+/PCX). X-ray photoelectron spectroscopy (XPS) was performed on the as-synthesized samples using a ESCALAB 250 XPS system with an Al Kα source (Thermo Fisher Scientific USA). UV-visible diffuse reflectance spectra were recorded using a UV-visible spectrophotometer with an

Table 1 Comparison of hydrogen evolution data of WS_2/MoS_2 composites compared with few of the literature reports

Photoelectrode	Light intensity (mW cm^{-2})	Electrolyte	Potential at −10 mA current density (*vs.* RHE)	Ref. (year)
SnO_2@MoS_2/FTO	150 W xenon lamp (400 nm cutoff filter, ~300 mW cm^{-2})	0.10 M Na_2SO_4 electrolyte solution	−0.73 V	61 (2017)
MoS_2@Cu_2O/FTO	A 350 W Xe arc lamp	Na_2SO_4 (0.1 mol L^{-1}, pH = 7) aqueous solution.	−0.47 mA at −1.5V *vs.* SCE	62 (2014)
Vertical WS_2 or MoS_2/SiO_2		0.50 M H_2SO_4	−0.34 or −0.41 V	63 (2016)
1T@2H–MoS_2/FTO	Visible light excitation	Na_2SO_4 (0.5 mol L^{-1})	−5 mA at −1.0 V *vs.* Ag/AgCl	64 (2016)
Vertical aligned WS_2/MoS_2/ITO	A 300W Xe arc lamp (CEL-HXF300) equipped with an ultraviolet cutoff filter (λ > 420 nm) ~100 mW cm^{-2}	0.50 M H_2SO_4	**−0.37 V**	This work
WS_2/MoS_2/Au	100 mW cm^{-2} using a 300 W Xe lamp as source with a cut-off filter (>420 nm, newport)	0.5 M H_2SO_4	−0.24 V	65 (2016)
WS_2/MoS_2 composites of nanosheets and quantum dots/GCE		0.50 M H_2SO_4	−0.26 V	66 (2015)
Vertical aligned WS_2/MoS_2/Ti		0.50 M H_2SO_4	**−0.21 V**	This work (ESI Fig. S6)

integrating sphere (Shimadzu UV2450, Japan). Photoluminescence measurements (PL) were carried out on a Hitachi F-4500 FL spectrophotometer at an excitation wavelength of 400 nm.

2.4. Electrochemical measurements

Electrochemical experiments were performed in a three-electrode cell in which a Pt plate and calomel were used as the counter and reference electrodes, respectively, and the as prepared samples were employed as the working electrode with an area of 0.16 cm^2. All the samples were analysed in 0.50 M H_2SO_4 solution (pH = 0.48). A 300W Xe arc lamp (CEL-HXF300) equipped with an ultraviolet cutoff filter (λ > 420 nm) was utilized as the visible light source with 150 mW cm^{-2} incident light intensity. Linear sweep voltammetry (LSV) with scan rate of 10 mV s^{-1} was conducted by an electrochemical workstation (CHI660E, Chenhua, China). All the potentials were transformed into the reversible hydrogen electrode (RHE) according to the Nernst equation:

E(*vs.* RHE) = E(*vs.* SCE) + 0.0591 pH + E^0_{SCE}. E^0_{SCE} = 0.245 V at 25 °C. EIS measurements were performed at an overpotential of −0.559 V *vs.* RHE over frequency range from 10^{-1} to 10^5 Hz. Electrochemical capacitance measurements were conducted by cyclic voltammetry (CV) for two cycles between 0.1 and 0.2 V *vs.* RHE with scanning rates of 60, 80, 100, 120 and 150 mV s^{-1}.

2.5. Photocatalytic activity measurement for HER

The photocatalytic H_2 production reactions of photocatalysts were carried out under open-circuit conditions (electron and hole transfer occur from the same electrode) using MoS_2/WS_2 layers fixed on an ITO support (8 cm^2). Specifically, the photocatalytic H_2 evolution is conducted in an outer irradiation-type photoreactor (Pyrexglass) connected to a closed gas-circulation system. The catalyst samples were put into 20 ml of aqueous solution containing 0.50 M H_2SO_4 solution. The catalysts were irradiated with a 300 W Xe arc lamp (CEL-HXF300). The photocatalytic H_2 evolution rate was analyzed with an online gas chromatograph (GC-7920, TCD detector).

3. Results and discussion

3.1. Structure characterization

SEM and HRTEM. SEM images of the pristine WS_2, pristine MoS_2 and MoS_2/WS_2 hybrid nanosheets are presented in Fig. 1. As shown in Fig. 1a–c, all the prepared samples are well distributed and vertically grown on the ITO substrate. Individual WS_2 or MoS_2 nanosheet was estimated to be dozens of nanometers in thickness, much thicker than that of MoS_2/WS_2 hybrid. The SEM images of MoS_2/WS_2 catalyst of different Mo : W ratios display similar morphologies (Fig. S1†). More details of the morphology and microstructure of the MoS_2/WS_2 hybrid nanosheets can be obtained from their TEM and HRTEM surveys shown in Fig. 2a–c. As revealed in Fig. 2b, a single MoS_2/WS_2 hybrid nanosheet consists of 2 to 10 layers, less than 10 nm, and each interlayer distance is characterized by ~0.62 nm (002). The lattice-resolved HRTEM image shown in Fig. 2c, enclosed by red boxes, and the corresponding FFT pattern indicate the highly crystalline characteristics and undoubtedly attributes to the hexagonal characteristics of the 2H–MoS_2 (upper right). In addition, the HRTEM image of the MoS_2/WS_2 hybrid nanosheets shown in Fig. 2c, enclosed by dark blue boxes, show some trigonal lattice area (octahedral coordination) of the 1T phase besides the common honey-comb lattice area of the trigonal prismatic coordination in the 2H phase. Nevertheless, the FFT of Fig. 2c (lower right) does not reveals the perfect hexagonal packing usually observed for 2H structure due to the overlap with the 1T structure. Furthermore, Raman spectra (Fig. S2†) show a set of characteristic peaks for MoS_2 nanosheets at 375 cm^{-1}, 403 cm^{-1} and 445 cm^{-1} arising from the E^1_{2g}, A_{1g} and longitudinal acoustic phonon modes,[52,53]

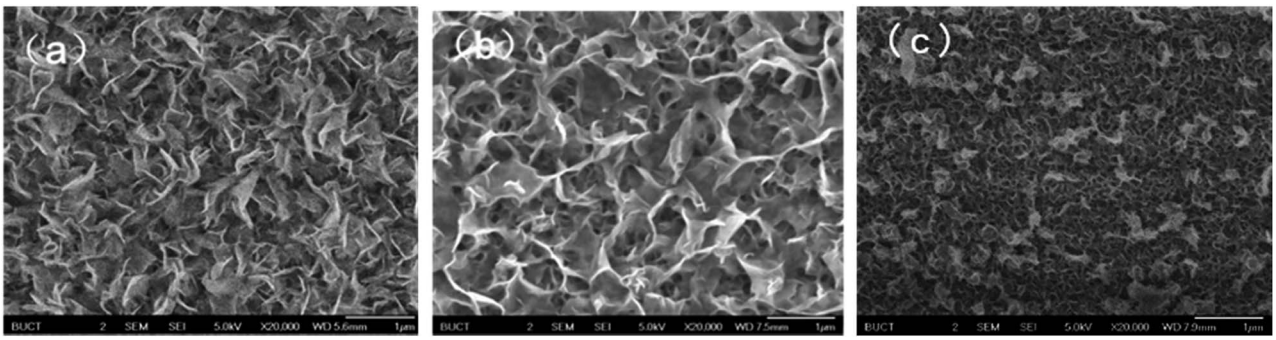

Fig. 1 SEM images of (a) WS_2, (b) MoS_2 and (c) MoS_2/WS_2 hybrid nanosheets. The calculated mole ratio of Mo : W is 1 : 1.

respectively, which corresponds to the presence of the 2H phase. The peaks at 220 cm^{-1} is ascribed to the 1T–MoS_2 phase, suggesting the existence of 1T phase ingredient embedded in the 2H–MoS_2 host.[54] 1T–MoS_2 nanosheets show higher HER catalytic activity than 2H–MoS_2 (ref. 12, 54 and 55) due to its metallic characteristics.[56] The fringe spacings of 0.27, 0.227, and 0.247 nm correspond to the (100), (103) and (102) planes of MoS_2, respectively.

The formation of 1T–MoS_2 is due to the intercalation of ammonia-ions, thus leading to the release of free 1T-MoS_2 nanosheets.[57] Nevertheless, the precursor of W source of $Na_2WO_4 \cdot 2H_2O$ is only beneficial to the formation of 2H structure[58]

Furthermore, we carried out elemental mapping and energy-dispersive X-ray spectroscopy (EDS) under scanning transmission electron microscopy (STEM) to probe the composition and spatial distribution of the constituent elements. Fig. 2d and e showed the intimate contact between WS_2 and MoS_2 by showing a perfect spatial correspondence and homogeneous S element distribution. More meaningful, the co-existence of the W and Mo element are both uniformly distributed with each other. The energy-dispersive spectrum (EDS) (Fig. 2e) of the hybrid confirms the coexistence of Mo, W and S, and the atomic ratio of S : Mo : W is 58.3 : 26.1 : 1.1, respectively. A relative small ratio of W indicates that the element of W doped MoS_2, and WS_2 is successfully implanted in the MoS_2 nanosheet matrix. However, the small ratio of W determined by EDS in the hybrid is obviously not consistent with the stoichiometric feeding ratio of 1/1. This is because Mo^{4+} and W^{4+} have difference in affinity to sulphur[59] The equilibrium constant of Mo-sulfidation is two orders of magnitude higher than that of W-sulfidation.[60,61] Therefore, the constituent proportion of MoS_2 is much higher than that of WS_2 in the composite.

XRD patterns. The X-ray powder diffraction (XRD) patterns of the as prepared samples confirmed the identity of the hexagonal WS_2 phase in all MoS_2/WS_2 samples (Fig. 3), and all the reflections at $2\theta = 14.3°$, 28.9° and 33.6° can be assigned to the (002), (004) and (101) planes of hexagonal WS_2 (JCPDS #84-1398), respectively. However, the characteristic peak for MoS_2 (002) was difficult to be distinguish from that of WS_2 due to their similar reflection position around 14.5°. In addition, the reflection for 1T phase of MoS_2, which generally showed typical peak splitting over (002), shifting to lower angles[57] is not detected. This is properly due to the fact that the content of 1T phase is too low to be detected by XRD technique.

The as-prepared MoS_2/WS_2 samples were further analyzed with XPS analysis (Fig. 4). The binding energies for each element are used to identify the individual elements due to their distinct values. In Fig. 4a, the XPS survey spectrum that Mo, W and S elements coexist in the surface elemental composition. Fig. 4b–d revealed a series of high-resolution XPS spectra of W 4f, Mo 3d, and S 2p. As presented in Fig. 4d, the S 2p peak splits into two peaks at 162.1 eV and 163.3 eV, which is corresponding to S $2p_{3/2}$ and S $2p_{1/2}$, respectively. Two peaks of Mo $3d_{3/2}$ at 232.9 eV and Mo $3d_{5/2}$ at 229.7 eV are typical characteristics of Mo 3d, and the other two peaks observed at 231.6 and 228.1 eV are ascribed to Mo $3d_{3/2}$ (1T) and Mo $3d_{5/2}$ (1T), respectively (Fig. 4c).

Two main peaks of W^{4+} in WS_2 are at the binding energies of 32.7 and 34.9 eV, which is the semiconducting prismatic 2H form.[62,63] Upon further scrutiny, W^{6+} was observed are at 37.3 eV, which are due to the presence of WO_3.[64]

Optical properties (PL and UV-vis). To investigate the visible-light absorption for the MoS_2/WS_2 hybrid nanosheets, we conducted an UV-visible absorption spectra experiment, as shown in Fig. 5a, and calculated the bandgap (E_g) of the as-prepared samples (Fig. S3†). For comparison, the light absorption and related E_g of the pristine WS_2 and MoS_2 are also included. According to UV–vis. spectra, all of the samples have absorption with wavelengths ranging from 350 to 600 nm (Fig. 5a). In comparison with the pristine WS_2 or MoS_2, MoS_2/WS_2 showed significantly increased adsorption intensity, and the MoS_2/WS_2 with Mo/W mole ratio of 1 : 1 exhibits the strongest adsorption. In addition, the resulting E_g values for WS_2, MoS_2 and MoS_2/WS_2(1 : 1) are 1.59, 1.80 and 1.67 eV, (Fig. S3†) respectively. In this context, both WS_2 and MoS_2 exhibit a small increase in the band gap, not well consistent with the theoretical bandgap of fewer layers WS_2 or MoS_2 (~1.3 eV). The increase in the band gap is properly attributed to the effect of the E_g of In_2S_3 (~2.4 eV) derived of ITO under hydrothermal condition (ESI Fig. S4†).

The PL spectra of MoS_2 and MoS_2/WS_2 were measured at an excitation wavelength of 400 nm to assess the separation efficiency of photogenerated electron–hole pairs. According to the PL spectra shown in Fig. 5b, the PL intensity of the MoS_2/WS_2 heterostructure is much weaker than that of MoS_2 or WS_2,

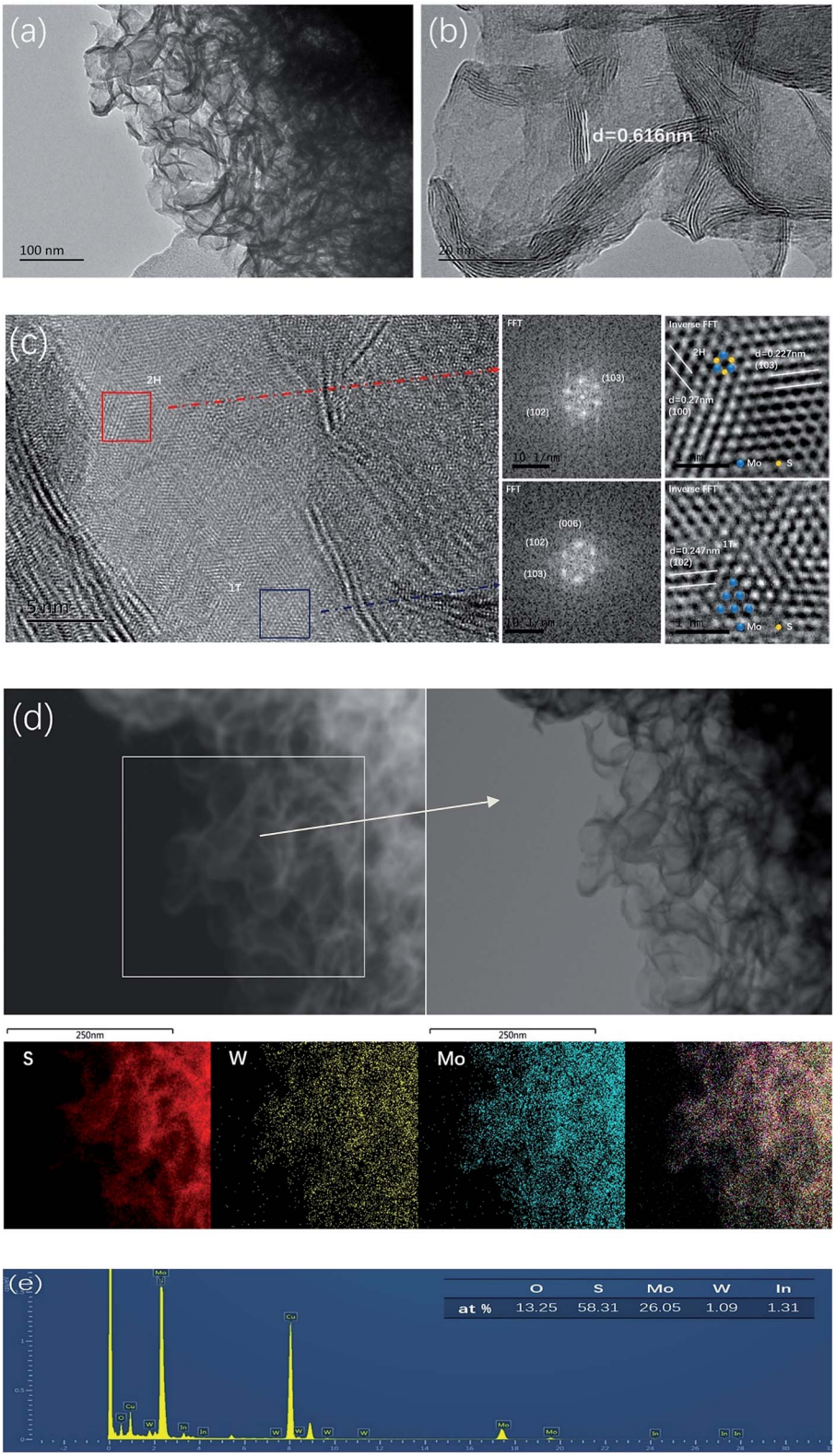

Fig. 2 (a) TEM images of MoS_2/WS_2, (b) HRTEM images, (c) HRTEM image of MoS_2/WS_2 with its corresponding Fast Fourier Transform (FFT), highlighting the random orientation of individual building blocks (evidenced by both the lattice fringes and the FFT ring pattern), (d) elemental mapping and (e) EDS spectrum of vertical aligned MoS_2/WS_2 structure. The calculated mole ratio of Mo : W is 1 : 1.

suggesting reduced recombination of photogenerated charge carriers under illumination. Apparently, the MoS_2/WS_2 heterostructure with mole ration of 1 : 1 shows the lowest PL intensity among all of the samples. With the reduced photogenerated charge carrier recombination and thus quick photogenerated charge carrier transportation and the interaction of the

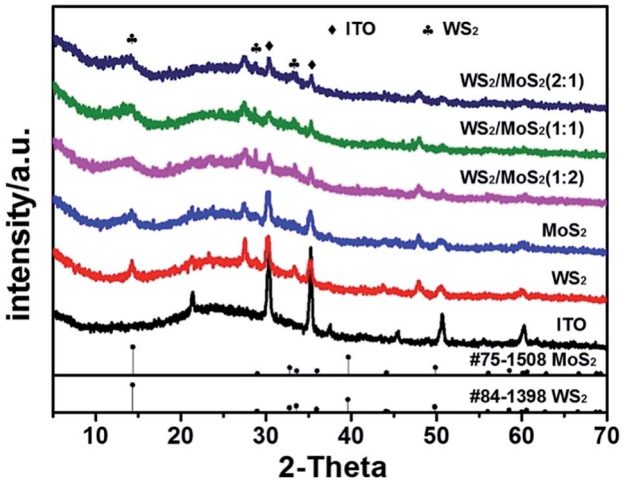

Fig. 3 XRD patterns of the as prepared samples.

photoinduced electrons with H^+ in water occurs directly, the as-prepared composite is anticipated to enhance the photocatalytic activity for HER.

To confirm the enhanced separation efficiency of photogenerated charge carriers, we measured the transient photocurrent (chronoamperometric) of the samples at bias of 0.372 V *vs.* RHE (Fig. 6). All of the samples exhibit good reproducibility of the photocurrent, and the intensity of MoS_2/WS_2 is much stronger than that of pristine MoS_2 or WS_2. The strongest photocurrent is obtained from the sample of MoS_2/WS_2 of 1 : 1. A higher photocurrent response of the composite suggests that heterostructures do has a higher separation efficiency of photogenerated electrons and holes.[65]

Additionally, operational stability is also an important criterion for a HER catalyst. To assess the stability of MoS_2/WS_2 for HER, a current density *vs.* time (*I*–*t*) curve was recorded over a longer reaction time (ESI Fig. S5†) at 0.372 V (*vs.* RHE). As shown in Fig. S5,† MoS_2/WS_2 (Mo/W = 1 : 1) electrode showed

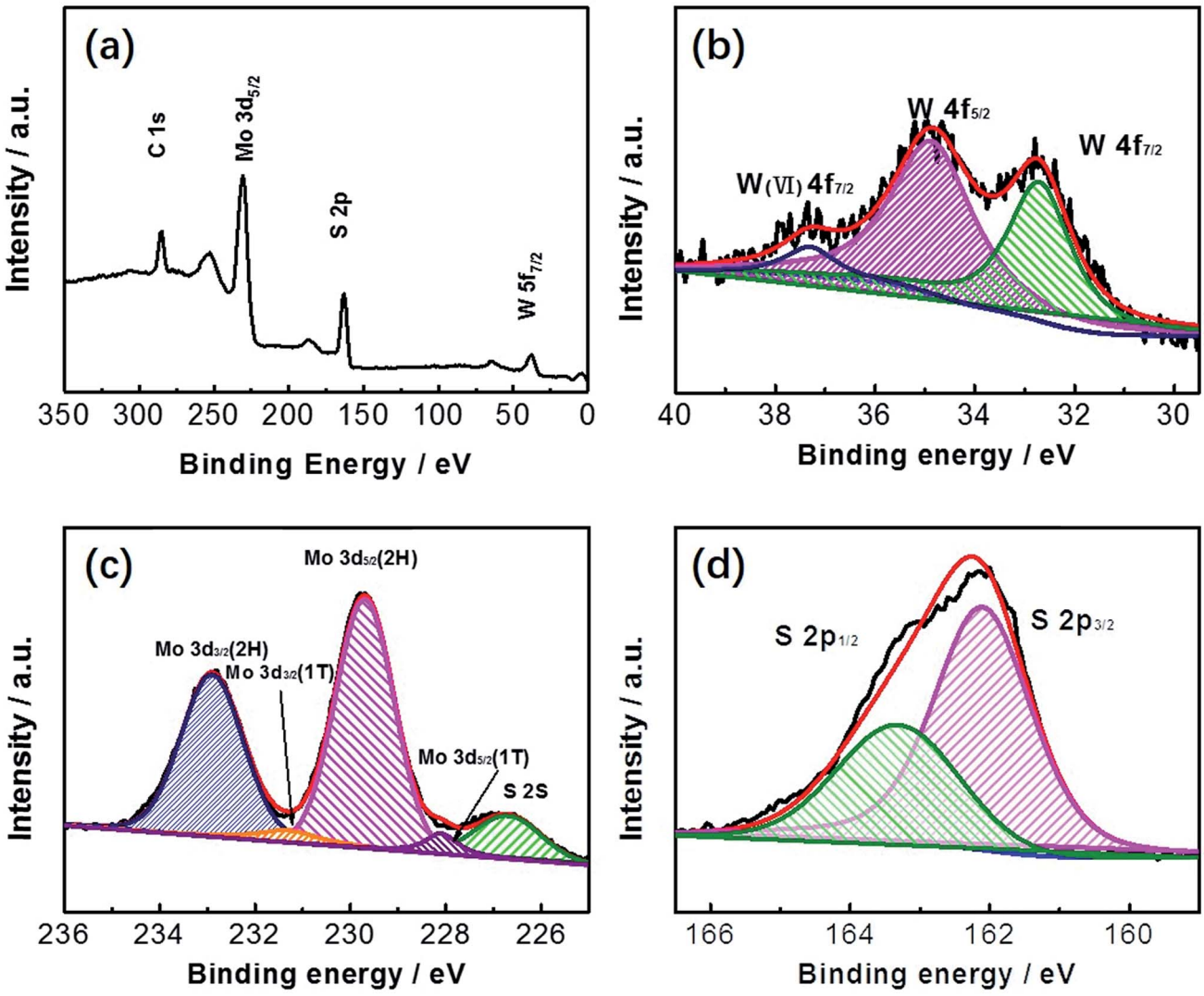

Fig. 4 (a) XPS spectrum of the MoS_2/WS_2 nanosheets, (b) high resolution XPS spectrum of Mo 3d, (c) high resolution XPS spectrum of W 3d, and (d) high resolution XPS spectrum of S 2p. The calculated mole ratio of Mo : W is 1 : 1.

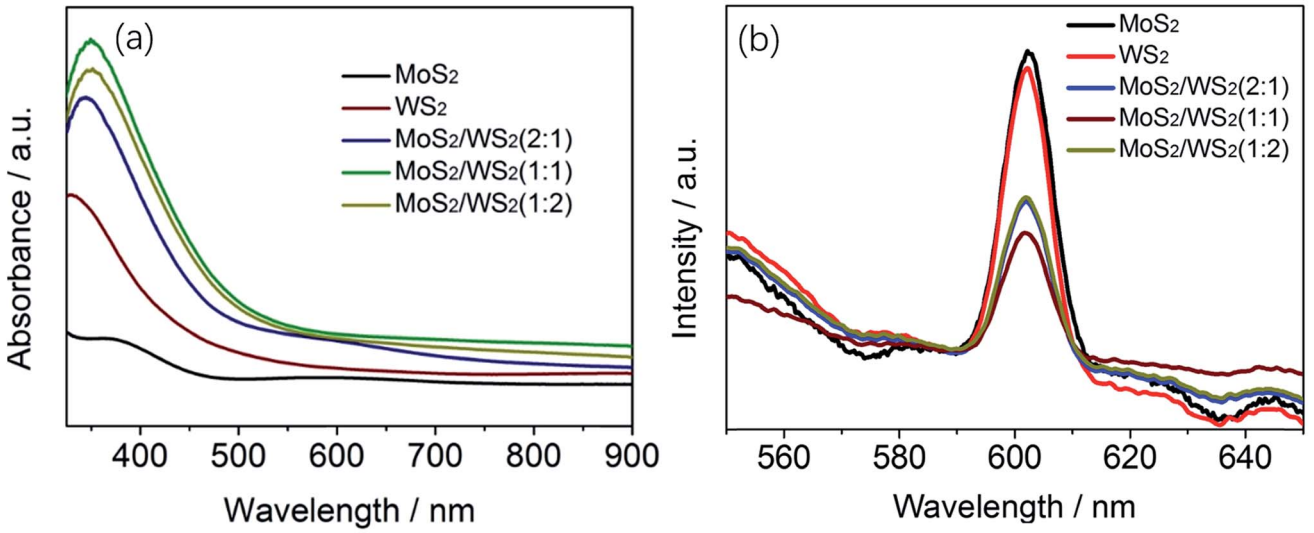

Fig. 5 (a) UV-visible absorption spectra of MoS_2/WS_2(1/1), (b) PL spectra of MoS_2/WS_2 nanosheets with different stoichiometric mole ratio of Mo : W.

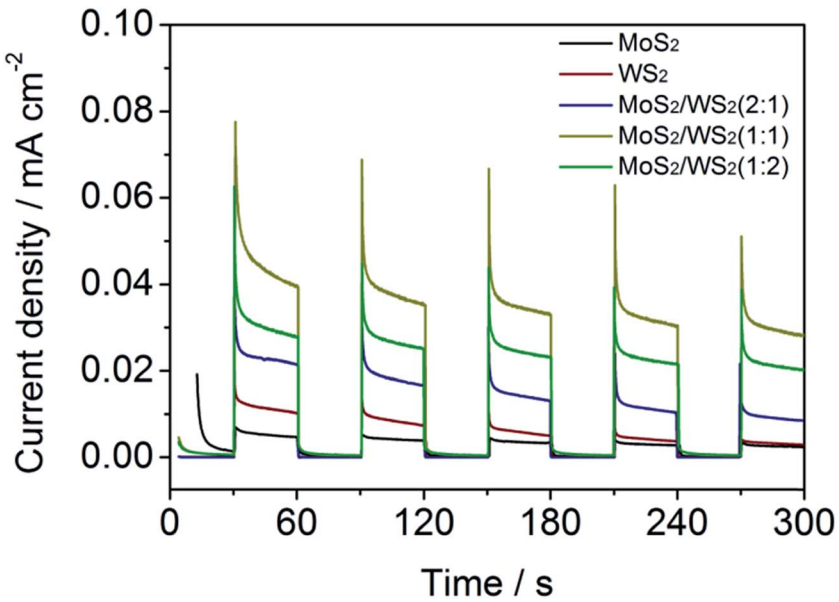

Fig. 6 On-off *J*–*t* curves of MoS_2/WS_2 vertically aligned structure of nanosheets prepared with different ratio of Mo to W precursor concentration at bias of 0.372 V *vs.* RHE in 0.5 mol L^{-1} H_2SO_4.

a photocurrent of ~0.04 mA in the initial stage of photo-irradiation, then decreased to 0.03 mA gradually and maintained the constant photocurrent for more than 7000 s.

Photoelectrocatalysis. The photoelectrocatalytic activity for HER performance of the MoS_2/WS_2 electrode was explored in 0.5 M H_2SO_4 solution using a three-electrode setup. For comparison, the HER activity of the as-prepared vertically aligned hybrid structures, including WS_2, MoS_2 and the MoS_2/WS_2 of different mole ratio of Mo : W, were investigated in dark or under light illumination (Fig. 7a). As shown in Fig. 7a, a standalone cathode of MoS_2 or WS_2 does not show noticeable cathodic current, whether in dark or under illumination condition. As expected, the cathodic polarization curves recorded for the vertically aligned MoS_2/WS_2 nanostructures exhibited a comparatively obvious photocurrent in comparison with that of standalone cathode of MoS_2 or WS_2, and shows greater current under light illumination than in the dark. In addition, the cathodic currents for all MoS_2/WS_2 samples are greater than the sum of the cathodic currents of pristine MoS_2 and WS_2, implying that the combination of MoS_2 and WS_2 in hybrid structures is synergistic rather than additive. The nanostructured MoS_2/WS_2 electrode (Mo/W ratio of 1/1) displays the highest current density among all the tested electrodes. Fig. 7b shows the differences in photocurrent density of the

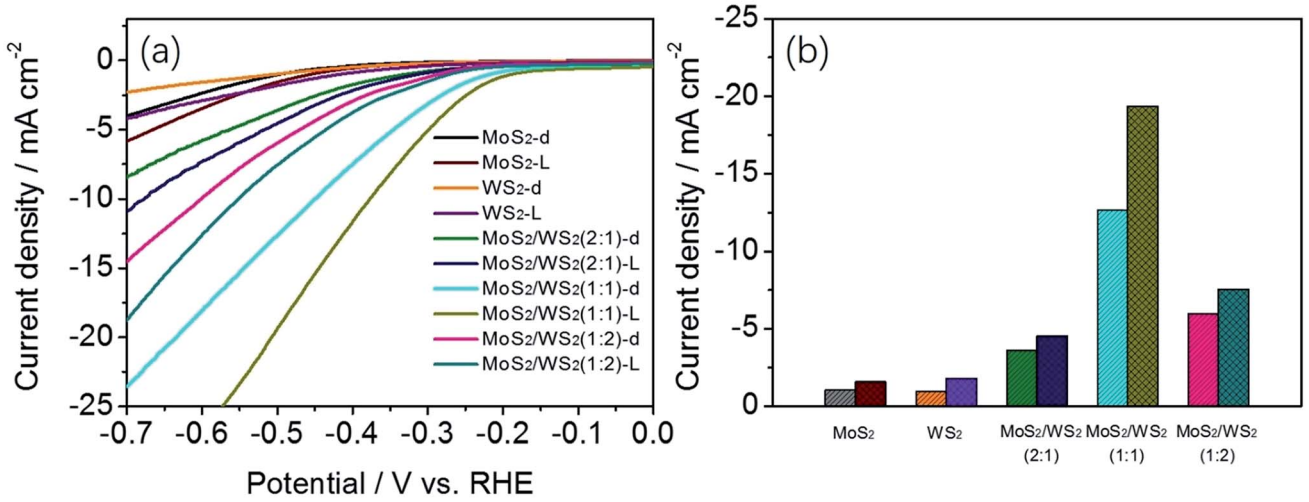

Fig. 7 (a) J–V curves of cathodic polarization of MoS_2, WS_2 and MoS_2/WS_2 catalysts and (b) histogram of current density at −0.5 V (*vs.* RHE) of MoS_2, WS_2 with different Mo : W ratios in dark and under simulated solar light (0.5 M H_2SO_4).

catalysts at the potential of −0.5 V *vs.* RHE, which is indicated by column charts for clarity. The corresponding Tafel slops are also evacuated, shown in Fig. S7.†

The photoelectrocatalytic activity for MoS_2/WS_2 hybrid was further evaluated by comparing its potential at −10 mA of photo-assistant current density with that from the related literature (Table 1).[66–71] They are comparable, since all these catalyst samples were prepared in form of ultrathin film on a less conductive substrate except Au and GCE. From the Table 1, we found that vertically aligned MoS_2/WS_2 hybrid shows a better photo assistant electrocatalytic activity on both less conductive and conductive substrate. This improvement in catalytic activity derives from the characteristics of the vertical aligned ultrathin MoS_2/WS_2 sheets that integrate energy band alignment and abundant active sites of MoS_2/WS_2 catalyst. We also highlighted the photocatalytic activity of MoS_2/WS_2 through photocatalytic H_2 production. The H_2 evolution rates

Table 2 Charge transfer resistance of MoS_2, WS_2 and MoS_2/WS_2 catalysts in dark and under simulated solar light for HER

	MoS_2-d	MoS_2-L	WS_2-d	WS_2-L	MoS_2/WS_2-d	MoS_2/WS_2-L
R_{ct}/Ω	55.21	54.66	80.49	65.60	23.13	17.92

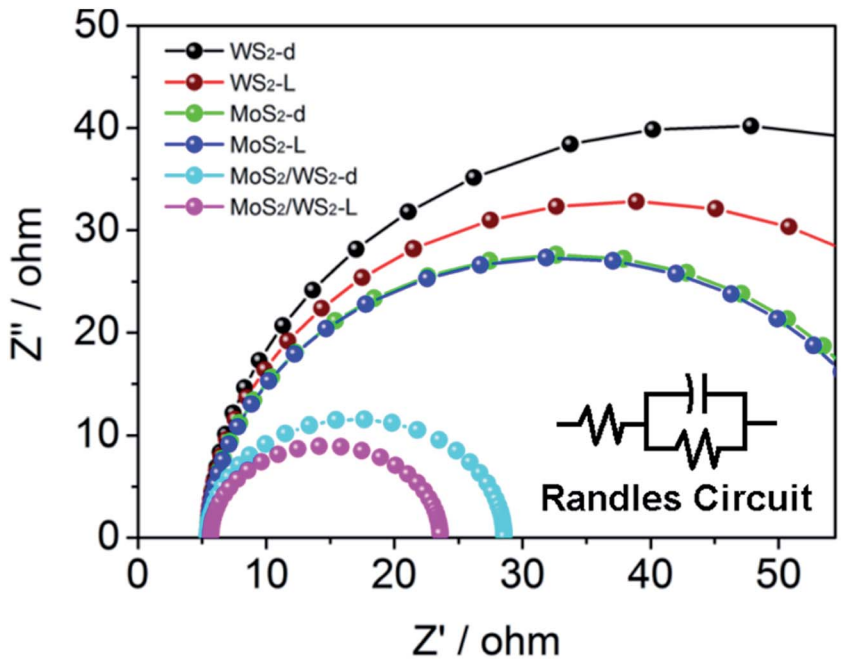

Fig. 8 AC impedance spectroscopy of MoS_2, WS_2 and MoS_2/WS_2(1 : 1) catalysts in dark and under simulated solar light.

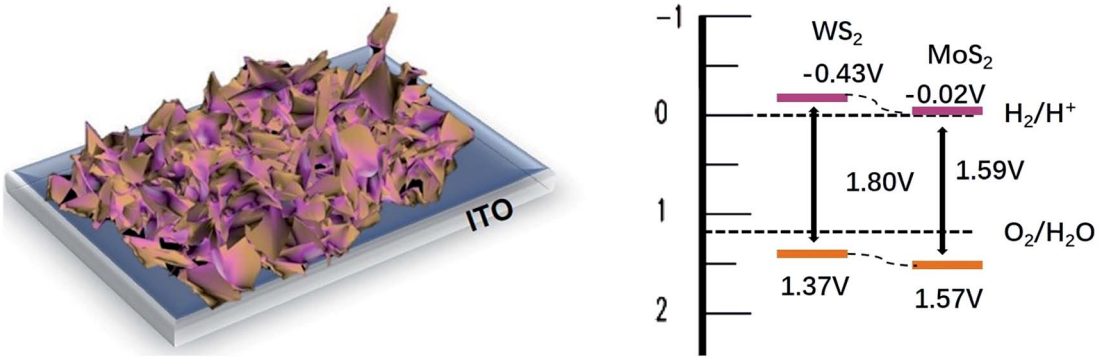

Scheme 1 Schematic illustrations of the charge transfer and separation on the MoS_2/WS_2 heterostructure under visible light. The energy band levels are calculated by the E_{CB} which is measured by flat-band potentials[75,76] and E_g values of WS_2 and MoS_2, as shown in Fig. S9a and b.†

under light irradiation without any applied bias for MoS_2/WS_2/ITO manifests the rate of 0.049 ml h^{-1}. It should be noted that the hydrogen evolution rate of 0.049 ml h^{-1} is produced from the ultrathin MoS_2/WS_2 layer of ~223 nm (Fig. S11†) which dispersed uniformly on the 8 cm^2 of surface area of ITO. For comparison with the previous studies, we have to convert ml h^{-1} to μmol g^{-1} h^{-1}, a customary unit used for hydrogen production rate. It was revealed that the MoS_2/WS_2 hierarchical nanosheet possesses significantly high photocatalytic activity (>2065 μmol h^{-1} g^{-1}). (ESI, Table S1†) noteworthy is, the estimated mass weight of MoS_2/WS_2 nanosheet is greater than the actual mass weight because the MoS_2/WS_2 structure is hierarchical and poriferous rather than solid, thus leading to an underestimate for H_2 evolution production.

Furthermore, the surface kinetics of the as prepared catalysts was evaluated by EIS (Fig. 8). The diameter of the fitted semicircle represents the charge transfer resistance (R_{ct}), which is inversely proportional to the rate of charge transfer in the HER process. In a Nyquist plot, the overlaying Nyquist plots of MoS_2/WS_2 (1/1) displayed a narrower semicircle diameter than that of WS_2 or MoS_2. In either case, in dark or under light illumination, the R_{ct} values of MoS_2 and WS_2 are found to be much higher than MoS_2/WS_2 (17.92 Ω and 23.13 Ω under light illumination and in dark, respectively) (Fig. 8). Compared to WS_2, or MoS_2, (see Table 2), the significantly reduced R_{ct} of MoS_2/WS_2 shows faster HER kinetics and better catalytic charge-transfer impedance. Undoubtedly, the faster HER surface kinetics of MoS_2/WS_2 produces a positive influence on photo- and electrocatalytic activity for HER.

We also measured the electrochemically active surface area (ECSA) of the solid–liquid interfaces through electrochemical double-layer capacitance (EDLC) of the catalytic surface *via* CV.[54] The EDLC values of MoS_2, WS_2 and MoS_2/WS_2 catalysts is 0.423, 0.245 and 3.05 mF cm^{-2}, respectively, which is obtained by the slop of a straight line extracted from the capacitive current as a function of scan rate.[72–74] As shown in Fig. S8c and f,† the EDLC value of 3.05 mF cm^{-2} for the MoS_2/WS_2 is much bigger than the values of MoS_2 and WS_2. (Fig. S8a–d and S8b–e,† respectively), indicating that MoS_2/WS_2 had the largest effective electrochemical area among the three catalysts, and thus presented more active sites.

Mechanism. Based on the above measurements, the enhanced photoelectrocatalytic activity of the MoS_2/WS_2 hybrid is attributed to the better electron transportation and higher electrochemically active surface area (ECSA), as well as the proper energy alignment. More importantly, when MoS_2 is coupled with WS_2, MoS_2/WS_2 hybrid showed a p–n junction characteristic of an inverted "V-shape" (see Fig. S9c†). The formation of p–n junction region between MoS_2 and WS_2 is beneficial to the separation of hole–electron pairs excited by photons. A representative structure of photoelectrode studied in this work, together with the relative simplified band diagram is demonstrated, as shown in see Scheme 1. When the heteronanostructure is constructed, the built-in electric field forms, and the hole–electron pairs, excited by photons, will immediately separate under internal electrostatic field in heterojunction region. Together with matching of band edges between WS_2 and MoS_2, MoS_2/WS_2 showed the improved photo-and electrocatalytic activity due to the restrained recombination. The best performance of catalyst for mole ratio of Mo/W of 1/1 is probably ascribed to compromise the contradictory relation between active sites and conductivity. (ESI Fig. S10†) in addition, uniquely designed electrode structure with the vertical array of the MoS_2/WS_2 ultrathin nanosheets brings in more active sites along with the optimized conductivity and reduced gas bubble adhesion, thus leading to high photoelectrochemical properties for HER.

4. Conclusion

MoS_2/WS_2 nanosheets with a vertically aligned structure fabricated directly on indium tin oxide (ITO) substrate were fabricated through a facile one-pot hydrothermal reaction. The hybrid nanosheets of MoS_2/WS_2 supplied numbers of active sites with proper defects since the elements of W doped MoS_2. Favorable band alignment, as well as high-quality, intimate p–n heterojunction between MoS_2 and WS_2, provides an effective carrier separation in this composite based photoelectric device. Therefore, the MoS_2/WS_2 nanosheets show better visible light activities than that of either pristine WS_2 or MoS_2 nanostructures. The improvements in both electro- and photocatalytic activities for HER are ascribed to the integration of

energy band alignment and abundant active sites derived of the vertically aligned MoS_2/WS_2 nanosheets. The rational use of the MoS_2/WS_2 cathode provided a new avenue toward achieving an enhanced electrocatalytic activity by photo-assistance.

Conflicts of interest

There are no conflict to declare.

References

1 C. Tsai, F. Abild-Pedersen and J. K. Norskov, *Nano Lett.*, 2014, **14**, 1381–1387.
2 A. Ejigu, I. A. Kinloch, E. Prestat and R. A. W. Dryfe, *J. Mater. Chem. A*, 2017, **5**, 11316–11330.
3 H. Huang, L. Chen, C. Liu, X. Liu, S. Fang, W. Liu and Y. Liu, *J. Mater. Chem. A*, 2016, **4**, 14577–14585.
4 H. Zhou, F. Yu, J. Sun, R. He, Y. Wang, C. F. Guo, F. Wang, Y. Lan, Z. Ren and S. Chen, *J. Mater. Chem. A*, 2016, **4**, 9472–9476.
5 D. A. Reddy, H. Park, S. Hong, D. P. Kumar and T. K. Kim, *J. Mater. Chem. A*, 2017, **5**, 6981–6991.
6 T. An, Y. Wang, J. Tang, W. Wei, X. Cui, A. M. Alenizi, L. Zhang and G. Zheng, *J. Mater. Chem. A*, 2016, **4**, 13439–13443.
7 Y. Xu, L. Wang, X. Liu, S. Zhang, C. Liu, D. Yan, Y. Zeng, Y. Pei, Y. Liu and S. Luo, *J. Mater. Chem. A*, 2016, **4**, 16524–16530.
8 Q. Wang, Z. Liu, X. Zhang, H. Zhao, C. Luo, H. Jiao and Y. Du, *J. Mater. Chem. A*, 2017, **5**, 9523–9527.
9 W. Maijenburg, M. Regis, A. N. Hattori, H. Tanaka, K. S. Choi and J. E. Ten Elshof, *ACS Appl. Mater. Interfaces*, 2014, **6**, 2003–2010.
10 Y. Yan, B. Xia, X. Qi, H. Wang, R. Xu, J. Y. Wang, H. Zhang and X. Wang, *Chem. Commun.*, 2013, **49**, 4884–4886.
11 Y. Yan, B. Xia, X. Ge, Z. Liu, J. Y. Wang and X. Wang, *ACS Appl. Mater. Interfaces*, 2013, **5**, 12794–12798.
12 D. Voiry, M. Salehi, R. Silva, T. Fujita, M. Chen, T. Asefa, V. B. Shenoy, G. Eda and M. Chhowalla, *Nano Lett.*, 2013, **13**, 6222–6227.
13 F.-K. Meng, J.-T. Li, S. K. Cushing, M. Zhi and N.-Q. Wu, *J. Am. Chem. Soc.*, 2013, **135**, 10286–10289.
14 G. Morales-Guio, S. D. Tilley, H. Vrubel, M. Gratzel and X. Hu, *Nat. Commun.*, 2014, **5**, 3059.
15 H. V. a. X. Hu, *ACS Catal.*, 2013, **3**, 2002–2011.
16 Y. Zhao, Y. Zhang, Z. Yang, Y. Yan and K. Sun, *Sci. Technol. Adv. Mater.*, 2013, **14**, 043501.
17 D. Merki and X. Hu, *Energy Environ. Sci.*, 2011, **4**, 3878.
18 S. Trasatti, *J. Electroanal. Chem.*, 1971, **33**, 350–378.
19 Sobczynski, A. Yildiz, A. J. Bard, A. Campion, M. A. Fox, T. Mallouk, S. E. Webber and J. M. White, *J. Phys. Chem.*, 1988, **92**, 2311–2315.
20 J. Bonde, P. G. Moses, T. F. Jaramillo, K. Nørskovb and I. Chorkendorff, *Faraday Discuss.*, 2009, **140**, 219–231.
21 A.-B. Laursen, S. Kegnæs, S. Dahl and I. Chorkendorff, *Energy Environ. Sci.*, 2012, **5**, 5577–5591.
22 Y.-G. Li, H.-L. Wang, L.-M. Xie, Y.-Y. Liang, G.-S. Hong and H.-J. Dai, *J. Am. Chem. Soc.*, 2011, **133**, 7296–7299.
23 J.-K. Lee, W. Lee, T.-J. Yoon, G.-S. Park and J.-H. Choy, *J. Mater. Chem.*, 2002, **12**, 614–618.
24 Q. H. Wang, K. Kalantar-Zadeh, A. Kis, J. N. Coleman and M. S. Strano, *Nat. Nanotechnol.*, 2012, **7**, 699–712.
25 D. Jing and L. Guo, *Catal. Commun.*, 2007, **8**, 795–799.
26 X. Zong, J. Han, G. Ma, H. Yan, G. Wu and C. Li, *J. Phys. Chem. C*, 2011, **115**, 12202–12208.
27 Y. Zhong, G. Zhao, F. Ma, Y. Wu and X. Hao, *Appl. Catal., B*, 2016, **199**, 466–472.
28 X. Zong, H. Yan, G. Wu, G. Ma, F. Wen, L. Wang and C. Li, *J. Am. Chem. Soc.*, 2008, **130**, 7176–7177.
29 K. Chang, Z. Mei, T. Wang, Q. Kang, S. Ouyang and J. Ye, *ACS Nano*, 2014, **8**, 7078–7087.
30 R. Tang, R. Yin, S. Zhou, T. Ge, Z. Yuan, L. Zhang and L. Yin, *J. Mater. Chem. A*, 2017, **5**, 4962–4971.
31 X. Hong, J. Kim, Su-F. Shi, Y. Zhang, C. Jin, Y. Sun, S. Tongay, J. Wu, Y. Zhang and F. Wang, *Nat. Nanotechnol.*, 2014, **9**, 682.
32 K. Chen, X. Wan, W. Xie, J. Wen, Z. Kang, X. Zeng, H. Chen and J. Xu, *Adv. Mater.*, 2015, **27**, 6431–6437.
33 H. M. Hill, A. F. Rigosi, K. T. Rim, G. W. Flynn and T. F. Heinz, *Nano Lett.*, 2016, **16**, 4831–4837.
34 K. Kośmider and J. Fernández-Rossier, *Phys. Rev. B: Condens. Matter Mater. Phys.*, 2013, **87**, 075451.
35 A. Kuc, N. Zibouche and T. Heine, *Phys. Rev. B: Condens. Matter Mater. Phys.*, 2011, **83**, 245213.
36 B. Hinnemann, P. G. Moses, J. Bonde, K. P. Jørgensen, J. H. Nielsen, S. Horch, I. Chorkendorff and J. K. Nørskov, *J. Am. Chem. Soc.*, 2005, **127**, 5308–5309.
37 H. Tributsch and B. B. Gesell, *Ber. Bunsen-Ges. Phys. Chem.*, 1977, **81**, 361–369.
38 H. Tributsch and J. C. Bennett, *J. Electroanal. Chem.*, 1977, **81**, 97–111.
39 B. Hinnemann, J. K. Nørskov and H. Topsøe, *J. Phys. Chem. B*, 2005, **109**, 2245–2253.
40 Z. Wu, B. Fang, A. Bonakdarpour, A. Sun, D. P. Wilkinson and D. Wang, *Appl. Catal., B*, 2012, **125**, 59–66.
41 D. Voiry, H. Yamaguchi, J. Li, R. Silva, D. C. Alves, T. Fujita, M. Chen, T. Asefa, V. B. Shenoy, G. Eda and M. Chhowalla, *Nat. Mater.*, 2013, **12**, 850–855.
42 C. L. Choi, J. Feng, Y. Li, J. Wu, A. Zak, R. Tenne and H. Dai, *Nano Res.*, 2013, **6**, 921–928.
43 X. Hai, W. Zhou, K. Chang, H. Pang, H. Liu, L. Shi, F. Ichihara and J. Ye, *J. Mater. Chem. A*, 2017, **5**, 8591–8598.
44 Y. Yu, S. Huang, Y. Li, S. Steinmann, W. Yang and L. Cao, *Nano Lett.*, 2014, **14**, 553–558.
45 Z. Lu, W. Zhu, X. Yu, H. Zhang, Y. Li, X. Sun, X. Wang, H. Wang, J. Wang, J. Luo, X. Lei and L. Jiang, *Adv. Mater.*, 2014, **26**, 2683–2687, 2615.
46 Y. Yan, B. Xia, Z. Xu and X. Wang, *ACS Catal.*, 2014, **4**, 1693–1705.
47 Y. H. Chang, F. Y. Wu, T. Y. Chen, C. L. Hsu, C. H. Chen, F. Wiryo, K. H. Wei, C. Y. Chiang and L. J. Li, *Small*, 2014, **10**, 895–900.

48 P. D. Tran, S. S. Pramana, V. S. Kale, M. Nguyen, S. Y. Chiam, S. K. Batabyal, L. H. Wong, J. Barber and J. Loo, *Chemistry*, 2012, **18**, 13994–13999.
49 J.-F. Xie, H. Zhang, S. Li, R.-X. Wang, X. Sun, M. Zhou, J.-F. Zhou, X.-W. Lou and Y. Xie, *Adv. Mater.*, 2013, **25**, 5807–5813.
50 S.-K. Park, D. Y. Chung, D. Ko, Y.-E. Sung and Y. Piao, *J. Mater. Chem. A*, 2016, **4**, 12720–12725.
51 N. Zhang, S. Gan, T. Wu, W. Ma, D. Han and L. Niu, *ACS Appl. Mater. Interfaces*, 2015, **7**, 12193–12202.
52 Y. Sun, K. Liu, X. Hong, M. Chen, J. Kim, S. Shi, J. Wu, A. Zettl and F. Wang, *Nano Lett.*, 2014, **14**, 5329–5334.
53 Q. Ding, F. Meng, C. R. English, M. Caban-Acevedo, M. J. Shearer, D. Liang, A. S. Daniel, R. J. Hamers and S. Jin, *J. Am. Chem. Soc.*, 2014, **136**, 8504–8507.
54 A. Lukowski, A. S. Daniel, F. Meng, A. Forticaux, L. Li and S. Jin, *J. Am. Chem. Soc.*, 2013, 10274–10277.
55 U. Maitra, U. Gupta, M. De, R. Datta, A. Govindaraj and C. N. Rao, *Angew. Chem., Int. Ed. Engl.*, 2013, **52**, 13057–13061.
56 Q. Liu, X. Li, Q. He, A. Khalil, D. Liu, T. Xiang, X. Wu and L. Song, *Small*, 2015, **11**, 5556–5564.
57 Q. Liu, X. Li, Z. Xiao, Y. Zhou, H. Chen, A. Khalil, T. Xiang, J. Xu, W. Chu, X. Wu, J. Yang, C. Wang, Y. Xiong, C. Jin, P. M. Ajayan and L. Song, *Adv. Mater.*, 2015, **27**, 4837–4844.
58 L. U. J. Bo, Z. Z. Wei and L. H. Gui, *China Tungsten Ind.*, 2005, **20**, 33–36.
59 G. Kulmukhamedov, A. Zelikman and G. Verevkin, *Zh. Anal. Khim.*, 1991, **36**, 2981–2985.
60 B. E. Erickson and G. R. HELZ, *Geochim. Cosmochim. Acta*, 2000, **64**, 1149–1158.
61 F. Wypych and R. Schöllhorn, *J. Chem. Soc., Chem. Commun.*, 1992, 1386–1388.
62 C. Liu, L. Wang, Y. Tang, S. Luo, Y. Liu, S. Zhang, Y. Zeng and Y. Xu, *Appl. Catal., B*, 2015, **164**, 1–9.
63 S. Li, S. Wang, D.-M. Tang, W. Zhao, H. Xu, L. Chu, Y. Bando, D. Golberg and G. Eda, *Applied Materials Today*, 2015, **1**, 60–66.
64 S. Hernandez, D. Hidalgo, A. Sacco, A. Chiodoni, A. Lamberti, V. Cauda, E. Tresso and G. Saracco, *Phys. Chem. Chem. Phys.*, 2015, **17**, 7775–7786.
65 J. O. M. Bockris and J. E. C. Potter, *J. Electrochem. Soc.*, 1952, **99**, 169–186.
66 X. Zhang, Y. Yang, S. Ding, W. Que, Z. Zheng and Y. Du, *Inorg. Chem.*, 2017, **56**, 3386–3393.
67 Y.-F. Zhao, Z.-Y. Yang, Y.-X. Zhang, L. Jing, X. Guo, Z.-T. Ke, P.-W. Hu, G.-X. Wang, Y.-M. Yan and K.-N. Sun, *J. Phys. Chem. C*, 2014, **118**, 14238–14245.
68 J. M. Woods, Y. Jung, Y. Xie, W. Liu, Y. Liu, H. Wang and J. J. Cha, *ACS Nano*, 2016, **10**, 2004–2009.
69 Y. Qi, Q. Xu, Y. Wang, B. Yan, Y. Ren and Z. Chen, *ACS Nano*, 2016, **10**, 2903–2909.
70 J. Shi, R. Tong, X. Zhou, Y. Gong, Z. Zhang, Q. Ji, Y. Zhang, Q. Fang, L. Gu, X. Wang, Z. Liu and Y. Zhang, *Adv. Mater.*, 2016, **28**, 10664–10672.
71 S. Xu, D. Li and P. Wu, *Adv. Funct. Mater.*, 2015, **25**, 1127–1136.
72 S. Trasatti and O. A. Petrii, *Pure Appl. Chem.*, 1991, **63**, 711–734.
73 J. D. Benck, Z. Chen, L. Y. Kuritzky, A. J. Forman and T. F. Jaramillo, *ACS Catal.*, 2012, **2**, 1916–1923.
74 R. Boggio, A. Garugati and S. Trasatti, *J. Appl. Electrochem.*, 1987, **17**, 828–840.
75 S. J. Hong, S. Lee, J. S. Jang and J. S. Lee, *Energy Environ. Sci.*, 2011, **4**, 1781.
76 H. Huang, D. Li, Q. Lin, W. Zhang, Y. Hao, Y. Chen, M. Sun and A. Fu, *Environ. Sci. Technol.*, 2009, **43**, 4164–4168.